Electrophysiological interaction through the interstitial space between adjacent unmyelinated parallel fibers

Roger C. Barr and Robert Plonsey
Departments of Biomedical Engineering, Pediatrics, and Cell Biology, Duke University, Durham, North Carolina 27706

ABSTRACT The influence of interstitial or extracellular potentials on propagation usually has been ignored, often through assuming these potentials to be insignificantly different from zero, presumably because both measurements and calculations become much more complex when interstitial interactions are included. This study arose primarily from an interest in cardiac muscle, where it has been well established that substantial intersitital potentials occur in tightly packed structures, e.g., tens of millivolts within the ventricular wall. We analyzed the electrophysiological interaction between two adjacent unmyelinated fibers within a restricted extracellular space. Numerical evaluations made use of two linked core-conductor models and Hodgkin–Huxley membrane properties. Changes in transmembrane potentials induced in the second fiber ranged from nonexistent with large intervening volumes to large enough to initiate excitation when fibers were coupled by interstitial currents through a small interstitial space. With equal interstitial and intracellular longitudinal conductivities and close coupling, the interaction was large enough (induced $V_m \sim 20$ mV peak-to-peak) that action potentials from one fiber initiated excitation in the other, for the 40-μm radius evaluated. With close coupling but no change in structure, propagation velocity in the first fiber varied from 1.66 mm/ms (when both fibers were simultaneously stimulated) to 2.84 mm/ms (when the second fiber remained passive). Although normal propagation through interstitial interaction is unlikely, the magnitudes of the electrotonic interactions were large and may have a substantial modulating effect on function.

INTRODUCTION

Extracellular potentials

The existence of extracellular potentials of significant magnitude has been recognized and utilized from the earliest investigations in electrophysiology. The presence of such potentials arising from cardiac muscle made possible such formative studies as those of Lewis and Rothschild (22) on cardiac excitation sequences, as well as the investigation of the intracellular–extracellular voltage and current relationships by Lorente de Nó (24) and others in nerves. In 1940 Katz and Schmitt (18) showed electrical interactions in vitro in a crab nerve preparation, and in 1941, Arvanitaki (1) defined the "ephapse" as the locus of close vicinity of two active membranes, and called transmission across such a site "ephaptic."

Nevertheless, the development of the penetrating microelectrode by Ling and Gerhard (23), which allowed investigators to measure intracellular potentials directly, greatly diminished the need to use extracellular potentials as indirect measures of transmembrane events. Thereafter, Hodgkin and Huxley (16), in their study of the nerve membrane, took advantage of the fact that extracellular potentials are small in comparison to intracellular potentials in most in vitro studies. Small extracellular potentials allowed them to equate transmembrane potentials to intracellular ones and to compute membrane currents as the second spatial derivatives of transmembrane potentials. This pattern has been followed in most analyses of experimental studies until the present because the structure of the experimental environment, which often involves a large conducting volume surrounding an active fiber, makes the assumption of near-zero extracellular potentials a good one.

Paradoxically, it is well known that substantial interstitial potentials exist in vivo, especially in cardiac muscle. Vander Ark and Reynolds (47) described potentials with magnitudes in excess of 50 mV within the ventricular wall. Spach and Barr (41) reported voltages that were tens of millivolts in potential maps of the canine heart. Kleber and Riegger (19) showed large extracellular potentials (equal to or greater than intracellular potentials) in rabbit papillary muscle under carefully controlled conditions, and Taccardi et al. (44) showed dramatic changes in observed extracellular waveforms of large magnitude based entirely on changes in the extracellular conducting paths. Studying the spinal motoneurons of the cat, Nelson (28) showed that facilitation of motoneurons can occur as a result of activation of other motoneurons. Recently, an extensive review of electrical

Address correspondence to Dr. Barr.

0006-3495/92/05/1164/12 $2.00

field effects and their relevance to central neural networks has been presented by Faber and Korn (10), especially as related to the mauthner cell.

In part because of the papers of Spach et al. (e.g., reference 42) on the importance of cellular discontinuities to propagation, the effects of all aspects of structure on propagation have received more systematic scrutiny in recent years. Nonetheless, the effects of substantial interstitial or extracellular potentials on propagation is a topic that has received much less attention, presumably because of the recognized importance of syncytial connections of the intracellular spaces of adjacent cells along with the technical difficulty of studying interstitial interactions. This technical difficulty arises experimentally because the greatest effects occur when cells or fibers are closely packed, producing the largest interstitial potentials but allowing the least access to electrodes. Specifically focused experimental design thereby is required, as in the work of Knisley et al. (20). In mathematical and numerical models, extracellular and interstitial studies also have been few. (Exceptions have included bidomain models [below], and significant recent studies such as Halter and Clark for myelinated nerve [13] and Leon and Roberge [21] showing velocity changes.) With models, the technical difficulty has been that mathematical analysis is simpler and numerical analysis is shorter when extracellular potentials are assumed to be zero.

Bidomain models

The one area of analysis that routinely has included interstitial potentials has been "bidomain" models, in which the averaged properties of intracellular and interstitial "domains" have been incorporated. Anticipated somewhat by Schmitt (39) in 1969 with his description of interpenetrating domains, Tung (46), Miller and Geselowitz (11, 26), and others took the viewpoint that, in spite of the actual discrete structure, the electrical events within cardiac muscle could be examined by regarding the tissue as a continuum (syncytium). Both intracellular space and interstitial space were considered continuous and described by the same coordinates, separated everywhere by the membrane. The same basic framework has been used, for example, by Muler and Markin (27) in a mathematical analysis, by Roberts et al. (36) in the ventricle, by Eisenberg et al. (9) as related to the lens of the eye, and by Roth (37) for cardiac muscle.

The results from bidomain models have made it clear that including interstitial potentials within the analysis leads to remarkable changes in propagation sequences compared with what one would have expected from simple extrapolation of one-dimensional analysis. Muler and Markin (27) showed remarkable isochrone patterns. Plonsey and Barr (2, 29) showed that the current flow patterns within the muclse would have multiple membrane transitions (rather than a simple local circuit with only two) and that, under extreme conditions, the shape of the excitation wavefront would deviate markedly from its expected elliptical shape. Wikswo and co-workers (40, 48) used bidomain analysis to show that stimulation of cardiac tissue can produce a virtual cathode, a dog-bone pattern of response to stimulation that arises from the anisotropic interstitial and intracellular conductivity.

Using bidomain analysis, Plonsey and Barr (30) argued on theoretical grounds that interstitial potentials rose quite rapidly with movement from the surface into the tissue, so that substantial interstitial potentials could be expected within a few cell diameters of the surface. Henriquez and Plonsey (14, 15) went on to show for cylindrical bundles that the traditional concept of a plane wave of excitation traveling down a bundle or block of tissue in contact with an external bathing solution could not be supported and that concave wavefronts were to be expected, a subject also explored by Roth (37).

These papers also show examples of a major shortcoming of the bidomain models: the scale of some of the emerging findings is the same as that of the discretization of the tissue formed by its cellular nature, so that the macroscopic averaging that underlies the bidomain formulation may not be justified. The bidomain model probably best portrays real tissue when it is extensive and healthy, since in these circumstances the interstitial potentials are largest and the uniformity assumed by the bidomain is greatest. In contrast, if one considers small numbers of active fibers, examines behavior when fibers are more loosely coupled, or seeks the potential field at a cellular (microscopic) level, a more sophisticated treatment is necessary. The goal of this paper is to investigate interstitial and extracellular effects so as to see how excitation is affected by each, but to avoid the averaging assumptions of the bidomain.

Model of two fibers

A central difficulty in conceiving a plan to investigate the effect of interstitial potentials on propagation has been the complexity of the experimental preparation or the model, which is the basis of a simulation. The problem intrinsically includes multiple regions that are simultaneously electrically active as well as the electrically conductive volume surrounding them (i.e., the extracellular medium) through which effects may be linked.

Knowing this, we sought a numerical preparation which retained the essential elements but was still

relatively simple, both in terms of geometric structure and related computational algorithms. This goal was achieved in the investigation of propagation in a two-fiber pair, within a restricted extracellular space. By varying the characteristics of the intervening extracellular volume, the interaction between extracellular and intracellular potentials, the effects of potentials generated by the one fiber on transmembrane potentials in the other, and the effects of the interaction on propagation could be investigated. Furthermore, as shown below, these steps could be accomplished within a context that was a direct (though not straightforward) extension of well-established methods and models frequently used and reported for studying one-dimensional propagation, an advantage in checking for errors as well as in differentiating results.

METHODS

Model structure

In concept, our goal was to evaluate interactions between two cylindrical fibers, A and B (Fig. 1), each with an intracellular (*IA* and *IB*) and surrounding extracellular (*EA* and *EB*) region. The extracellular region was limited in extent.

A widespread practice in electrophysiology has been to represent an individual cylindrical fiber as if it were purely one-dimensional by means of a core-conductor model. Extending this idea, we used two linked core-conductor models to represent the fiber pair. In the linked model (Fig. 2), there were two core-conductor models, one for fiber A (top half) and one for fiber B (bottom half). As is conventional, the core-conductor model for each fiber represented the intracellular region as a series of axial resistances in one dimension (e.g., R_{IA}), the extracellular region similarly described (e.g., R_{EA}), and intracellular-to-extracellular interconnections described by discrete units (*open rectangles*) assigned membrane properties. Departing from convention, for the two fibers we linked their two core-conductor grids through a series of extracellular resistors (e.g., R_{EC}), representing the connection through the common extracellular region. The resulting model clearly

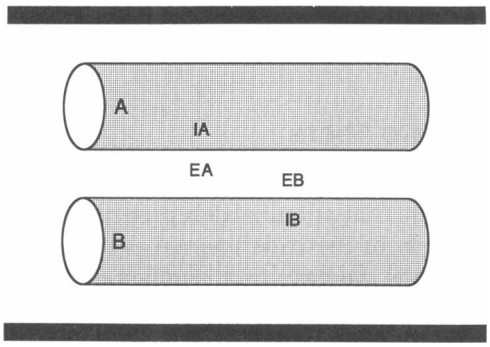

FIGURE 1 Paired fibers. Two fibers, *A* and *B*, are represented by cylinders, within a restricted extracellular space. *IA* and *IB* identify intracellular space for fibers *A* and *B* respectively, and *EA* and *EB* identify portions of the extracellular volume near *A* and *B*.

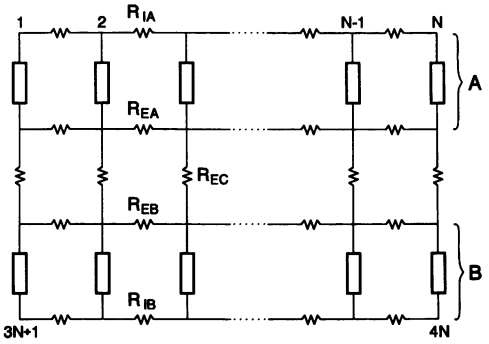

FIGURE 2 Resistive grid to represent paired cylinders. To a good approximation, the electrical properties of the paired cylinders can be represented by this resistive grid. The rectangles are membrane elements. Resistances R_{IA} and R_{IB} are along intracellular paths; R_{EA}, R_{EB}, and R_{EC} characterize the extracellular space. Points where lines join are referred to as "nodes," and the nodes are numbered from 1 to N across the top row, $N + 1$ to $2N$ on the second row, up to $4N$ in all. In the calculations shown below, N was set to 200, and the fiber length was set to 10 space constants.

was not a complete representation of the full three-dinensional electrical characteristics of the paired cylinders of Fig. 1. At the same time, it retained essential characteristics: a separately active fiber *A* and fiber *B*, an extracellular volume linking the two, and a means of varying the degree of linkage through changing the resistances R_{EA}, R_{EB}, and R_{EC} of the extracellular region.

In the results, two specific cases held particular interest. In the first case, the two fibers were considered widely separated. For this case, Fig. 3 *I* shows the pattern of relative conductances (conductances being the reciprocals of the resistances of Fig. 2) that were used. In case 1, the total longitudinal extracellular conductance, taking the two paths EA and EB in parallel, was 100 times the conductance of either intracellular axial conductance. In case 1, one would expect the interaction of fibers *A* and *B* to be small and the results to be quite close to those for a single fiber. In contrast, in case 2 the fibers were

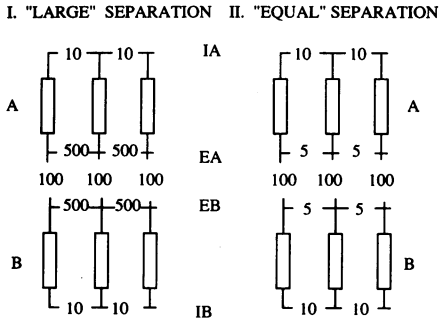

FIGURE 3 Two particular choices for grid values for the resistive grid of the paired cylinder problem. Numbers given are the relative conductances (reciprocal resistance), and are scaled before use to the actual fiber diameters. In *I* the longitudinal extracellular pathways have high conductance (as in a tissue bath), whereas in *II* the extracellular pathways have low conductance (fibers close together). Note that otherwise the conductance patterns are the same.

close together. The total longitudinal conductance, again taking EA and EB in parallel, was equal to that of either fiber's intracellular longitudinal conductance.

In converting these conductance ratios into a specific numerical prototype, we used a fiber radius $a = 40$ μm, $R_i = 100$ Ω-cm, and $C_m = 1.0$ μF /cm^2, values adapted from those used in an analysis of the cardiac conduction system (33). The longitudinal intracellular and extracellular conductances of cases 1 and 2 occur if one considers each fiber to have circular cross-section with diameter $2r$ located within an extracellular region with square cross-section and side length 8.5% $> 2r$, located within a nonconductor. The linkage conductances were not determined geometrically but rather were chosen to reflect the extremes of moving the extracellular regions apart (case 1, linkage conductance one-tenth of the longitudinal) or together (case 2, linkage conductance 10×). It is worth noting that once the linkage conductances become very large (or very small) in relation to the longitudinal ones, the precise value of the linkage conductance is not very significant since the longitudinal conductances dominate. These numerical values were useful in forming a simplifed example, but caution is in order in extrapolating the results to measured results from any tissue, because both differences in the conductances of the surrounding tissue and the actual (three-dimensional) structure of the extracellular volume are potentially significant, as well as changes in the parameter values themselves.

From a theoretical perspective, the linked core-conductor representation can be expected to be valid so long as the transverse extracellular dimensions are small compared with each fiber's length constant, since this condition validates a one-dimensional treatment. An exception, which is considered here as case 1, is where the separation is large, in which case the situation reduces to two uncoupled fibers. Then each behaves according to the classical case of low extracellular potential, so that $\Phi_i - \Phi_e \approx V_m$ in view of $\Phi_e \approx 0$. In this case the intracellular behavior will be represented correctly, but the distributed extracellular volume will not be represented accurately.

One should also note that the behavior described by Fig. 2 at the ends of each fiber coresponds to an open circuit condition. Thereby the total axial currents must be equal in magnitude to the total transmembrane current in the discrete membrane element at the end.

Mathematical and numerical methods

An outline of the mathematical and numerical methods is given in Table 1. Most algorithms that find action potentials (that is, that find V_m as a function of time) operate in the sequence of Table 1 A. Specifically, one begins with a knowledge of the transmembrane current density, I_m, everywhere, at a certain time t. From the set of values of I_m one finds new values for V_m at a slightly later time $t + \Delta t$. (Often the initial values of I_m are zero, as a baseline, and then change to nonzero values with an applied stimulus.) Explicit and implicit methods for the time extrapolation have been widely utilized. The new values of V_m for time $t + \Delta t$ then are used to get new values for the membrane state (parameters such as m and h for the sodium channels), and for intracellular potential Φ_i (Table 1 A, step 3). (So doing is facilitated by the network of Fig. 2.) The new values for Φ_i can be spatially differentiated to get new values for I_m (Table 1 A, step 4). Repeating this cycle generates a series of values of V_m (or the other variables) as a function of time.

Simple $V_m - \Phi_i$ relationships

In many problems, computation of Φ_i can be shortened or omitted entirely. As outlined in Table 1 B, there are three cases of interest. In the first (Table 1 B, case 3a), the extracellular potentials are small enough that they can be ignored. That is, $\Phi_i \approx V_m$. (This is the assumption used for analysis of most in vitro experiments, where active tissue is surrounded by a large extracellular volume.) In the second case (3b), the extracellular potentials may be large, but the problem is entirely one-dimensional, so Φ_i is proportional to V_m. While the proportionality has to be taken into account, the computation is short: the one-dimensionality leads to the linear core-conductor equations, and $\Phi_i = r_i/(r_i + r_e)$, where r_i, r_e are the intracellular and extracellular axial resistances per unit length (31). Consequently, Φ_i is immediately obtained from V_m. This case applies for fibers in oil, (e.g., reference 24).

TABLE 1 Numerical methods

Compute		From
A Sequence		
1. $V_m(t + \Delta t)$		$I_m(t)$
2. Membrane gating, e.g., $m(t + \Delta t)$		$V_m(t + \Delta t)$
3. $\Phi_i(t + \Delta t)$		$V_m(t + \Delta t)$
4. $I_m(t + \Delta t)$		$\Phi_i(t + \Delta t)$
Repeat steps 1 to 4, moving from $(t + \Delta t)$ to $(t + 2\Delta t)$, etc.		
Extracellular Space	$\lvert\Phi_e\rvert$	Computation
B Detail for step 3 of sequence		
3*a* Large	Small	Short, since $\Phi_i^t \approx V_m^t$
3*b* Small but 1D	Large	Short, since $\Phi_i^t \sim V_m^t$ (core conductor)
3*c* Small	Large	Long, since $\Phi_i^t \sim \int_V (\partial^2 V_m^t/\partial x^2)/f(r)\, dV$
C Restatement of 3*c* in discretized (matrix) form $[\Phi(t)] = [M_{ij}][V_m^t(j)]$, where $i = 1, \ldots, 2N$ and j likewise, and N = the number of node points along a single fiber ($2N$ total for a pair).		

More complex $V_m - \Phi_i$ relationships

In the third case (Table 1 B, case 3c) the simulation is considerably more complex. The complexity arises because, when the interstitial potentials are large, and when excitation is not one dimensional, there is no simple relationship between Φ_i and V_m. Unless simplifying assumptions apply, the resulting relationship between Φ_i and V_m will show that Φ_i at a single point (and I_m at a point) will depend on V_m everywhere.

Matrix formulation for grid

For the two-fiber problem, the resistive grid of Fig. 2 was used to represent the intracellular and extracellular regions. For the resistive grid, we considered the problem of how to find Φ_i and Φ_e at all nodes, given a set of values for V_m at a particular time. The solution to this problem was found using conventional circuit analysis, namely, by creating and then solving a set of simultaneous linear equations, where the number of equations equaled the number of nodes. In so doing it was useful to number the nodes from 1 to N along the top row of Fig. 2, from $N + 1$ to $2N$ along the second row, and similarly for all four rows, giving $4N$ nodes in all. Equations then were created in three ways.

First, a set of $2N$ equations defined transmembrane potentials V_m at each node pair crossing a membrane, e.g.,

$$\Phi_i^2 - \Phi_e^2 = \phi^2 - \phi^{N+2} = V_m^2, \quad (1)$$

where the lower case ϕ is used to signify the potential at the particular

node, without distinguishing whether the node is intracellular or extracellular, and the superscript identifies the particular node as defined in Fig. 2.

Second, a set of $2N - 1$ equations arose from the requirement that the current entering the membrane from node k equal the current leaving the membrane into node $N + k$ (continuity of current), and that the total node current at k and $N + k$ be zero, e.g.,

$$2G_{IA}\phi^2 - G_{IA}\phi^3 - G_{IA}\phi^1 + (2G_{EA} + G_{EC})\phi^{N+2} - G_{EA}\phi^{N+3} - G_{EA}\phi^{N+1} - G_{EC}\phi^{2N+2} = 0, \quad (2)$$

for the membrane transition from node 2 to node $N + 2$, and where conductance G is the reciprocal of resistance R, e.g., $G_{EA} = 1/R_{EA}$.

Third, one equation determined the reference potential. To keep the results symmetric from fiber A to B and end to end, we chose the reference potential as the average potential at all four extracellular endpoints, i.e.,

$$\phi^{N+1} + \phi^{2N} + \phi^{2N+1} + \phi^{3N} = 0. \quad (3)$$

The set of $4N$ equations that resulted was stated conveniently in matrix form,

$$[A][\phi] = [V], \quad (4)$$

where matrix A was the set of coefficients arising from Eqs. 1–3 above, and ϕ was a column vector of the potentials at all nodes. V was a column vector with the top $2N$ values equal to V_m at each membrane element (from equations like 1 above) and the bottom $2N$ entries equal to zero (from equations like 2 and 3 above). Inversion of matrix A produced

$$[\phi] = [A]^{-1}[V]. \quad (5)$$

In Eq. 5, only the left $2N$ columns of $[A]^{-1}$ matter, since the columns to the right would be multiplied by the zeros in vector $[V]$. Further, since finding Φ_i (but not Φ_e) was required to get I_m, half the rows of Eq. 5, corresponding to nodes for a Φ_e value, could be discarded. (Rows for a few extracellular points were retained separately to find wave forms at those sites.) With these reductions, Eq. 5 was restated as

$$[\Phi_i] = [M][V_m], \quad (6)$$

where $[M]$ is the remainder of matrix $[A]^{-1}$ after half the rows and half the columns were discarded.

Eqs. 1–3 arise from the same physical considerations used previously for bidomain calculations, where exact analytical relations are given (29). The result in the bidomain was

$$\Phi_i(x,y) = \frac{1}{4\pi}\int_V \left[g_{ox}\frac{\partial^2 V_m}{\partial x'^2} + g_{oy}\frac{\partial^2 V_m}{\partial y'^2}\right] \cdot \log\left[\frac{(x-x')^2}{g_{ix}+g_{ox}} + \frac{(y-y')^2}{g_{iy}+g_{oy}}\right] \cdot \frac{dx'dy'}{\sqrt{(g_{ox}+g_{ix})}\sqrt{(g_{oy}+tg_{iy})}}, \quad (7)$$

where the g's are bidomain conductivities (29). Eq. 7 for the analytical bidomain is the analogue of Eq. 6 for the grid. Note that an integral over the whole volume is required to find the potential at a single point, an analogue to the matrix multiplication.

Calculation length

Results below are shown for $N = 200$. The fact that a matrix M must be used to find Φ_i from V_m complicated and lengthened the process of finding action potentials. For $N = 200$, V_m was specified at $N = 200$ points along each fiber, so 400 values of V_m were present in total. Matrix M therefore was 400 by 400. Three problems had to be addressed. First, finding matrix M required the inversion of matrix A, an 800 by 800 ($4N$ by $4N$) matrix. Second, to find V_m as a function of time, a matrix multiplication (Table 1 *B*, step 3c) had to be completed at each time transition, i.e., thousands of times. For increasing N, this part of the calculation quickly came to dominate the overall execution time, because it involved more steps than those required for membrane transitions (which otherwise were limiting). Third, the conditions for stability were different than for simple core-conductor problems; i.e., arguments based on the mesh ratio no longer applied in the same way. The calculation tended to be more unstable. All three factors were significant, but tractable.

Membrane model

In the calculations done here, each membrane element was assigned Hodgkin–Huxley (16) properties. Hodgkin–Huxley membrane properties were used because they were relatively simple computationally and allowed both depolarization and repolarization effects to be seen in strands of short spatial dimensions.

Numerical methods

A space constant λ first was determined from the expression $\lambda = \sqrt{r_m/(r_i + r_e)}$, where r_m is the membrane resistance times length, and r_i and r_e were the intracellular and extracellular resistances per unit length, respectively. (31, p. 127) Values used were those for fiber A. Second, interval Δx between nodes was chosen so that the one space constant corresponded to 20 nodes. The 200 nodes along the length of the fiber thereby made the fiber 10 space constants long, both for case I and case II. Because λ varied between these cases, the absolute fiber length in millimeters also varied. Third, making use of the definition of the mesh ratio as $\Delta t/(r_i c_m \Delta x^2)$ (31, p. 116), we then assigned a value to interval Δt which made the mesh ratio equal to 0.1. Having been derived for one-dimensional current flow, neither the space constant nor the mesh ratio had the same significance in case 2 as in case 1. The extension of their use to case 2 thereby was arbitrary but proved satisfactory in practice.

For case 1, $\lambda = 0.17$ cm, $\Delta x = 0.00851$ cm, and $\Delta t = 0.369$ μs. For case 2, $\lambda = 0.0992$ cm, $\Delta x = 0.00496$ cm, and $\Delta t = 0.369$ μs.

Computer methods

Calculations reported here were accomplished with two FORTRAN programs of ~800 lines each. The first program made use of information about the fiber structure and produced matrix M of Table 1 *C*. The second used this matrix and computed potentials as a function of time. Program development and initial executions were completed on a personal computer (IBM PS/2 model 70/486, IBM Corporation, Research Triangle Park, NC), operating under AIX to allow larger arrays of data. When the simulations grew from small test cases to those reported here, time required for execution of the second program grew to ~12 h on this machine. To allow the series of final calculations to be done more quickly, the programs were transferred to the Cray YMP at the North Carolina Supercomputing Center, located in Research Triangle Park, NC, where they were compiled and executed remotely using the Center's network access.

RESULTS

Coupling coefficients

The degree of interaction between the fibers was reflected by the numerical values of the entries in matrix M of Eq. 6. For illustration, consider the single scalar value Φ_i^{100}, the intracellular potential at the center of fiber A. $\Phi_i^{100}(t)$ was found as $\Sigma_j M_{100,j} V_m^j(t)$, so the entries in row 100 of matrix M determined how Φ_i at the center of fiber A originated from V_m everywhere, at a particular time. Table 2 shows selected elements of row 100 of matrix M.

The top portion of Table 2 identifies which of the 400 columns of matrix M have been extracted for the table. (Other columns were not extracted because the value of the element was near zero.) As identified in the top third of Table 2, the columns selected were those corresponding to the ends of fiber A (elements 1 and 200), the middle of fiber A (98–102), the ends of fiber B (201, 400), and the middle of fiber B (298–302). Although all columns came from a single row of matrix M, the column values are arranged on two rows in Table 2 to better suggest their relative geometric positions in Fig. 2. The top third of Table 2 gives the specific arrangement of the columns.

The middle third of Table 2 gives the values of elements of matrix M for large extracellular conductivity (Fig. 3, case 1). The entries of Table 2 showed that Φ_i^{100} was determined almost solely from V_m at the same site (coefficient of 0.983), not being affected significantly either by V_m at adjacent sites on the same fiber (coefficients of 0.002) or by V_m at the adjacent site on fiber B (coefficient of −0.003). The coefficient was 0.983 rather than 1 because case 1 included extracellular resistances that, while small, relative to the intracellular ones, were not zero.

The bottom third of Table 2 shows coupling coefficients for equal extracellular conductivity (Fig. 3, case 2). Here Φ_i^{100} had a weaker relationship with V_m at the same site (coefficient of 0.626), a much stronger relationship to V_m of fiber B at the adjacent site (coefficient of −0.292), and an increased dependence on V_m at adjacent sites on the same and opposite fibers (coefficients with magnitude of 0.019). Additionally, there was a significant contribution from the ends of either fiber (coefficient of 0.167). The end effect did not diminish when the length of the fiber was extended from 100 to 200 elements.

Physical reasoning suggests that potentials Φ_i should depend mainly on values of V_m nearby. Inspection of the pattern of numerical values within matrix M confirms in part that this is the case, because Φ_i at position 100 depends strongly on the transmembrane potentials from fibers A and B at the same axial position. Nonetheless, there remains a significant end effect, a consequence of the restricted extracellular volume. It also is noteworthy that the great majority of entries in matrix M are still virtually zero.

For both cases 1 and 2, note that the sum of the entries along row A of Table 2 is one. The consequence was that, in the absence of a contribution from fiber B, a uniform V_m along fiber A produced the same intracellular potential at the center of fiber B for either case. In contrast, the sum of the entries along row B is zero, so that a uniform V_m along fiber B had no effect on Φ_i at the center of fiber A, in both cases.

Large extracellular conductance (I), in time

With large extracellular conductance, one expects there to be little interaction between fibers and expects propagation down either fiber to be essentially unchanged from that of a single isolated fiber. That such is the case is seen in Fig. 4. (Note the vertical displacement between the traces for fiber A, plotted against the scale on the *left,* and the traces for fiber B, plotted against the scale on the *right.*) Transmembrane potentials (V_m) are shown as a function of time at positions 10 and 100 on fiber A (designated $a10$ and $a100$) and corresponding sites on fiber B. Site 10 is near the left end, and site 100 is in the middle. As expected, a 1-ms transmembrane

TABLE 2 Sample coupling coefficients from row 100 of matrix *M*

	Numbers of the nodes with corresponding values presented below.								
A	1	...	98	99	100	101	102	...	200
B	201	...	298	299	300	301	302	...	400
	Values of elements in Matrix *M* for 1. Large extracellular conductivity								
A	0.005	...	0.001	0.002	0.983	0.002	0.001	...	0.005
B	0.005	...	−0.001	−0.002	−0.003	−0.002	−0.001	...	0.005
	Values of elements in matrix *M* for 2. Equal extracellular conductivity								
A	0.167	...	0.001	0.019	0.626	0.019	0.001	...	0.167
B	0.167	...	−0.001	−0.019	−0.292	−0.019	−0.001	...	0.167

The node numbers correspond to columns in matrix M. Nodes 1–200 lie on fiber A, whereas 201–400 are on B.

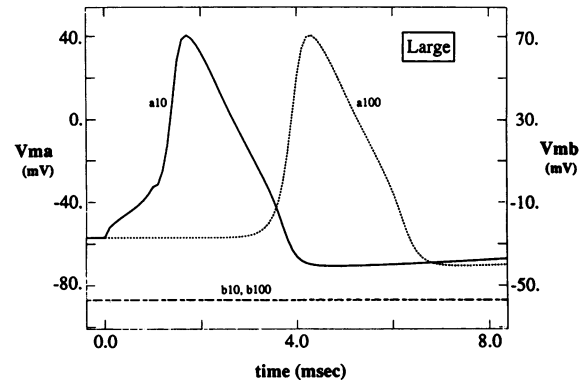

FIGURE 4 Action potentials for large extracellular volume, i.e., large extracellular conductance. Fiber A was stimulated at node 10. Simulated action potentials for nodes 10 and 100 of fiber A ($a10$ and $a100$) are plotted against the left vertical axis; APs for nodes 10 and 100 of fiber B ($b10$ and $b100$) are plotted against the right vertical axis. Node 10 is near the left end, and node 100 is in the middle. The baselines are offset to allow easier visualization of the individual waveforms.

stimulus (beginning at $t = 0$) applied to fiber A at $a10$ produced an action potential at $a10$ and, after a delay, a similar action potential at $a100$. Fiber B was not stimulated, and no action potentials occurred at $b10$ or $b100$.

Equal extracellular conductance (II), in time

Active fiber *B*

Quite different results occurred when the pattern of equal conductances of Fig. 3 II was used. With equal conductances, when fiber A (only) was stimulated at site $a10$, action potentials occurred both in fiber A and in fiber B, as shown in Fig. 5. In that figure, note that action

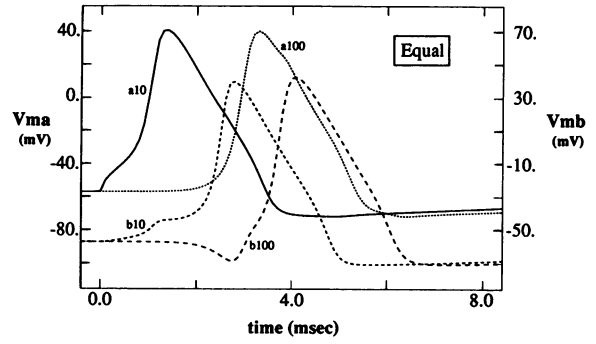

FIGURE 5 Action potentials for extracellular resistance equal to intracellular. As in Fig. 4, node 10 of fiber A was stimulated, but no stimulus was applied to fiber B. Action potentials began in fiber B because of the interaction through the extracellular volume. Waveforms for fiber A (B) are plotted against the left side (*right*) axis.

potentials occurred at $a10$ and then $a100$, as before. In addition, action potentials occurred at $b10$ (the site on fiber B across from $a10$ on fiber A), and later at $b100$. (As in Fig. 4, the action potentials for fibers A and B again were displaced vertically for greater visibility.) The action potentials in fiber B occurred even though there was no intracellular linkage between fibers A and B. (There was the possibility of excitation of fiber B occurring through numerical error in the simulation, but extensive checking did not show evidence of such an error.) A number of interesting details can be observed in Fig. 5. For example, in the varying waveshapes among the four sites, note the longer delay at $a10$–$b10$ compared with $a100$–$b100$, and the hyperpolarization at $b100$ that precedes the upstroke.

Passive fiber *B*

As shown above, the equal conductance pattern produced action potentials in both fibers A and B soon after the onset of the stimulus to A. Active responses in both fibers began during the stimulus. The question arose as to whether the events in fiber B were primarily a result of the stimulus, which, although applied to A, also was coupled to B, or primarily the result of some other facet of the initiation of excitation in fiber A that would not be present once stable propagation was established.

To consider this possibility, the intracellular and extracellular conductances were maintained but the membrane conductances of fiber B were not allowed to vary with time for 3.3 ms after the onset of the stimulus. (Approximately 3.3 ms was required for propagation three-fifths of the distance down the fiber.) That is, for 3.3 ms the computer simulation forced fiber B's membrane to retain its resting membrane ionic conductivities, so that fiber B remained passive during this interval.

Action potentials again were calculated (Fig. 6). In fiber A, action potentials at $a10$ and $a100$ were similar to those before. In fiber B, V_m showed deflections at $b10$ and $b100$ at the time of the corresponding upstrokes in

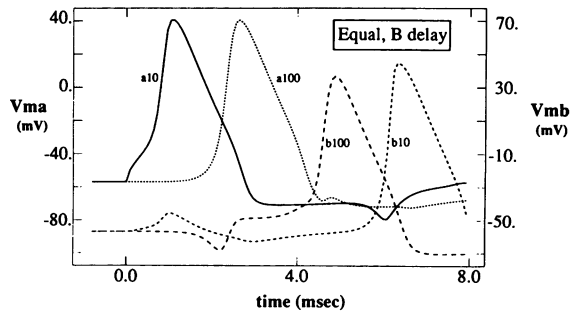

FIGURE 6 Action potentials for extracellular resistance equal to intracellular, with fiber B passive for 4 ms. Otherwise the same as Fig. 5.

fiber A. When fiber B was allowed to become active at 3.301 ms, excitation began in fiber B, leading to an action potential at $b100$. Then excitation propagated in a retrograde direction so that the action potential at $b10$ occurred later than the action potential at $b100$. This result showed that initiation of action potentials in fiber B was not simply a direct effect of the stimulus current.

Large extracellular conductance (I), in space

The nature of the interaction between fibers A and B with the equal conductance pattern is difficult to understand using waveforms plotted versus time, since the interaction is primarily a spatial one. For reference, a spatial distribution is plotted in Fig. 7 for large extracellular conductance, at a time when propagation had proceeded about halfway down fiber A. The figure shows that both V_m and Φ_i had a sharp upstroke to the right, the direction of propagation, and that they had virtually equal amplitude. In contrast, Φ_e had an amplitude close to zero. Both Φ_i and V_m for fiber B maintained constant resting values everywhere.

Equal extracellular conductance (II), in space

Active fiber *B*

With equal extracellular conductances (Fig. 8), waveforms were quite different. In fiber A, Φ_i now had a reduced amplitude and different waveshape from V_m in the same fiber. Φ_e, plotted on the same amplitude scale, was no longer near zero. The action potentials V_m and Φ_i in fiber B, shown in the bottom part of Fig. 8, were dissimilar to each other and to the corresponding plots for fiber A.

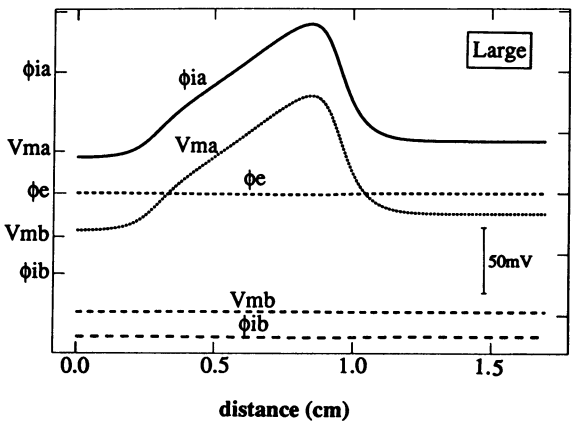

FIGURE 7 For large extracellular conductance, the transmembrane, intracellular, and extracellular potentials vs. distance for the paired fiber problem are shown. ϕ_{ia}: intracellular potential for fiber A; V_{ma}: transmembrane potential for fiber A; ϕ_e: extracellular potential; V_{mb}: transmembrane potential for fiber B; ϕ_{ib}: intracellular potential for fiber B. Each waveform is plotted using the same vertical calibration. For visibility on the figure, plots are displaced vertically to the point shown by the tic mark on the left axis for each waveform. Note that the mark identifies the zero-level, which is usually not the resting level.

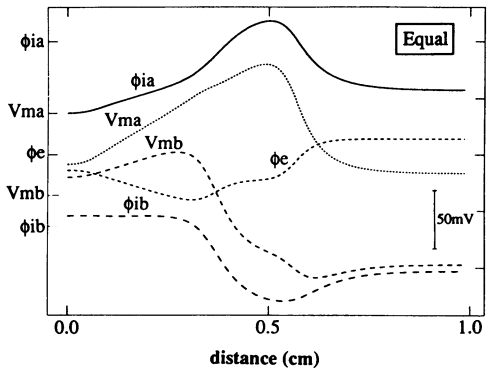

FIGURE 8 For extracellular conductance equal to intracellular, the same spatial plots as those of Fig. 6 are shown. Now ϕ_e is significantly larger than zero, and action potentials are induced in fiber B.

Because the structural change from Fig. 7 to Fig. 8 was the different extracellular conductance pattern, it was clear that the large differences must have arisen from that source, either directly or indirectly. The interacting spatial and temporal events were so complicated, however, that it was difficult to separate cause from effect. Therefore, we also looked at the spatial distribution with fiber B passive.

Passive fiber *B*

With fiber B kept passive for 3.301 ms, the spatial distribution was plotted at 3.3 ms (Fig. 9). In fiber A, Φ_i and V_m continued to differ, but the difference was not as much (as in Fig. 8). Φ_e was still significantly nonzero, although with a smoother waveshape. In fiber B, moving from the resting region into the excited region (*right* to *left*), V_m was first hyperpolarized by 11.8 mV (*right*) and then depolarized by 8.6 mV (*left*) over a distance of ~2 mm centered at 0.6 cm. There was a concave shape of Φ_i versus distance, with a minimum near the center.

With fiber B passive, it constituted a modest passive RC load to fiber A (rather than an active load), and the relationship between ϕ_{ia}, ϕ_{ea}, and v_{ma} (lower case signifies deviation from resting values) was close to that expected in a bounded isolated fiber described by the linear core-conductor model. That is, $\phi_{ia} \approx r_i v_{ma}/(r_i + r_e)$ and $\phi_{ea} \approx -r_e v_{ma}/(r_i + r_e)$ (31, p. 111), if the intracellular path of fiber B was included in determining r_e.

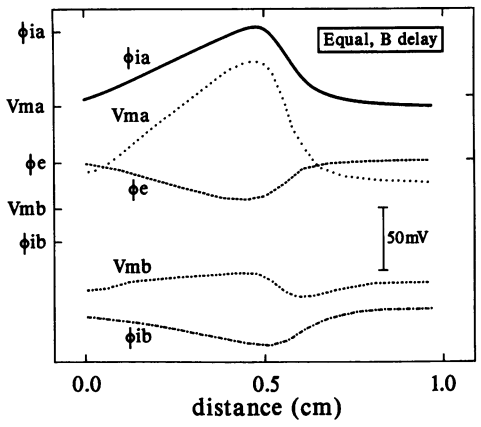

FIGURE 9 For extracellular conductance equal to intracellular, but fiber *B*'s membrane not allowed to become excited (i.e., held with its resting properties), the same spatial plots as those of Fig. 6 are shown. Note that the presence of extracellular potentials induces marked deviations from baseline values in both V_{mb} and ϕ_b.

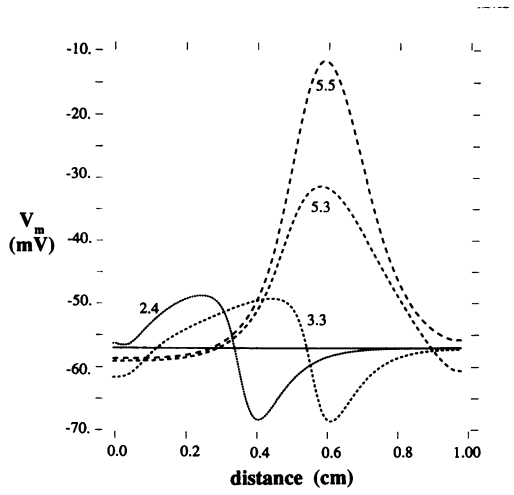

FIGURE 10 Evolution of activation in fiber *B*. *A* series of spatial distributions of V_m in fiber *B* (only) is shown. Each line portrays V_m vs. distance along the fiber, for one time. The number beside each line is the time in milliseconds (measured from the start of the stimulus) for that line.

Fiber *B* after release

Inspection of the shape of the Φ_i curve for fiber *B* suggests how current flows within fiber *B*. Fiber *A* induced a concave spatial distribution of Φ_i in fiber *B*. The concave waveshape caused intracellular current to flow toward the voltage minimum of Φ_i. The resulting outward membrane current might be considered a stimulus. Inspection of the curve for V_m shows how fiber *B* becomes excited. Fiber *A* induced a depolarization of sufficient magnitude (8.6 mV) to initiate activation once fiber *B* was allowed to respond, with a significant latency because the voltage change was near threshold. The action potentials in fiber *B*, beginning just after 3.3 ms, were the result.

The evolution of fiber *B* through passive and active phases can be seen by plotting V_m versus distance along the fiber at several instants (Fig. 10). Activation in fiber *A* at 2.4 ms induced V_m in *B*, as shown by the line labeled 2.4. From 2.4 to 3.3 ms, fiber *B* was passive, as activation progressed along fiber *A*. Accordingly, the distribution of V_m in fiber *B* at 3.3 ms is similar to that at 2.4 ms, translated to the right. Fiber *B* became active just after 3.3 ms, and by 5.3 ms the potential distribution had an entirely different shape, with the most positive potentials (near 0.6 cm) well above threshold. These potentials grew more positive rapidly, as seen by the distribution at 5.5 ms.

It is interesting to observe that the site of earliest activation ($\approx$6 mm) was further down the fiber than the site of most positive transmembrane potential when fiber *B* became active at 3.3 ms ($\approx$4 mm). This spatial shift appeared to be the consequence of continued propagation in fiber *A* occurring concurrently with the time required for the active changes in the membrane of fiber *B* to produce an action potential.

Propagation velocity

The propagation velocity in fiber *A* away from the ends was measured from the simulated wave forms for three cases (Table 3). Cases 1 and 2 were the same as described above. For case 2, the velocity measurement was obtained when fiber *B* was passive. Case 3 used the same intracellular and extracellular conductance pattern as case 2. In case 3 both fiber *A* and fiber *B* were stimulated simultaneously, and thereafter excitation proceeded identically in both fibers. Column *C* of Table 3 gives the simulated velocity in each case. The results showed a substantial decrease in conduction velocity between cases 1 and 2, reflecting the diminished extracellular conductance. A further substantial decrease occurred between cases 2 and 3, even though there was no further reduction in the extracellular conductance.

TABLE 3 Propagation velocities

A Case	*B* Condition	*C* Velocity	$D\ r_e/r_i$
		mm/ms	
I	*A* active	2.84	=0.02
II	*A* active, *B* passive	2.28	$\approx$0.65
III	*A* and *B* stimulated	1.66	$\approx$2.0

Column *D*: Case 1, as in simulation. Cases II, III from relative velocities.

Linear core-conductor theory (31, p. 117) associates changes in velocity with changes in resistivity. That theory states that

$$\frac{\theta_2}{\theta_1} = \sqrt{\frac{[r_i + r_e]_1}{[r_i + r_e]_2}}, \quad (8)$$

where r_i and r_e are the intracellular and extracellular resistances per unit length, and the subscripts identify the cases compared. We used this relationship and the ratio of r_e/r_i for case 1 to predict a value for r_e/r_i for cases 2 and 3, with the results given in Table 3, column *D*. These results show that the linear core-conductor model predicts the velocity in case 2 if the extracellular resistance per unit length is a little greater than would be provided by the parallel combination of both extracellular pathways of Fig. 2 plus the intracellular pathway along fiber *B*. The velocity observed in case 3 is predicted correctly if the extracellular volume is conceptually divided into two parts, with half associated with fiber *A*.

DISCUSSION

Model limits

It is important to keep in mind that all of the results presented here arise from a model, so that this study shows directly only the properties of the model itself, rather than those of any real tissue that the model might appear to approximate. Further, the focus in model construction was on a clean and relatively simple structure for examining interactions in the absence of geometric complications. As a result, the model is not a detailed representation of the structure of any real tissue, nerve or muscle. At the same time, the modeling of fibers as cylinders has become so common, and the results often so useful, that further insight into the properties of the model is interesting in its own right and possibly useful in suggesting explanations for measurements from real tissue.

When extracellular space is sufficiently reduced in volume to permit ephaptic effects between two fibers, the possibility also exists of other interactions, such as accumulation of potassium. Such effects might be particularly notable if the rate or rhythm of excitation changed or if it differed markedly from one fiber to the other. Only electrical interactions were included in this study, however, mainly because understanding electrotonic interaction in the absence of other changes was considered the primary goal. An important corollary benefit of limiting the goals in this way was that a less complex series of calculations had to be completed.

Passive and active responses

In the two-fiber model with fiber *A* active, a division can be found between events in fiber *B* due to its passive properties, and its subsequent active response. As shown by Fig. 6 (voltage vs. time), with equal extracellular conductance the coupling through the extracellular space induced in fiber *B* first a hyperpolarization and then a depolarization, with a positive voltage change of ~ 20 mV in < 1 ms. These voltages were induced because of biophysical properties of the second fiber as a part of the volume conductor surrounding fiber *A*. As such, their magnitude and time course was a consequence of extracellular and intracellular resistances and the membrane capacitance but was not controlled by the active responses of the membrane model. The fact that passive interaction must take place has been recognized for some time, and the work of Markin (25) and Clark and Plonsey (4) in the early 1970s showed possible ways modeling this interaction.

With the Hodgkin–Huxley model used, fiber *B* responded to the induced currents by initiating action potentials in fiber *B*. Because the induced transmembrane stimulus involved hyperpolarization and then depolarization, the spatial change in the intracellular potential of ~ 20 mV was considerably greater than the depolarization from the resting level, about half that much. Our results provide no direct information about the nature of the responses that quite different models, such as those of Drouhard and Roberge (6) or DiFrancesco and Noble (5) for cardiac tissue, might produce. At the same time, the similar nature of the sodium current in all these models, as well as the magnitude of the transmembrane voltages induced, makes it likely that some kind of active response would be present. It is clear that the details of the response will depend on the interaction of depolarizing and repolarizing responses near the resting voltage.

It also was evident from the results that the presence of fiber *B* changed the time course of events in fiber *A*, in part through the changes in the passive properties of fiber *A*'s extracellular volume. The most visible changes occurred when fiber *B*'s action potentials generated the same changes in *A* that fiber *A* had earlier generated in *B*; only the relatively refractory state of *A* prevented a reactivation of *A* and a possibly oscillating sequence from being established.

Electrotonic interactions

So little has been established on a quantitative basis about extracellular coupling that there is as yet no sound basis for delineating those in vivo contexts where it might play a significant role. A number of disorders

involving the interaction of nerves, such as hemifacial spasm (38) and trigeminal neuralgia (12), have been discussed in terms of ephaptic transmission, and such transmission has been demonstrated experimentally in the squid giant axon (34) and cardiac ventricular cells in vitro (43). Present-day understanding suggests that most if not all normal action potential propagation is by means of other mechanisms.

On the other hand, a substantial body of work has shown that electrotonic interaction between active cells can have a substantial modulating effect on function. In cardiac electrophysiology, for example, recent work by Roberge et al. (35) showed the importance of electrotonic interactions for near-threshold stimuli, Tan and Joyner (45) examined electrotonic influences on action potentials in ventricular cells, and Joyner et al. (17) examined effects of tissue geometry on cardiac action potential initiation. The magnitudes of the interactions through interstitial couplings shown here are well beyond the magnitudes shown to have an effect.

An example of the strong electrotonic interaction is in the velocity data presented in Table 3. Both case 2 (fiber A active) and case 3 (fibers A and B simultaneously active) have the same pattern of conductance, and fiber A is excited in the same way, yet fiber A shows markedly different conduction velocities. In case 2, fiber A's velocity is that to be expected if extracellular current from fiber A uses all extracellular paths and, to a lesser degree, fiber B's intracellular path. In contrast, in case 3 fiber B has "taken back" its own intracellular path and half the extracellular path, so that fiber A's velocity is markedly diminished.

Magnitude of interaction

One of the most informative aspects of the simulation is that it provides a detailed, quantitative example of the magnitudes of the induced effects for a particular degree of extracellular coupling. Loosely stated, when the extracellular resistivity was equal to the intracellular resistivity of either fiber, the induced passive voltage changes were in the range of 10 mV hyperpolarization and 10 mV depolarization, although there was a complicated temporal and spatial distribution. These magnitudes declined to almost zero, as expected, when the extracellular conductivity was large. Conversely, even larger voltages would be induced if the fraction of the total volume that was intracellular increased beyond half. Such higher packing fractions are suggested by the high extracellular voltages reported by several investigators, making plausible the induction of changes in vivo of even greater extent.

The authors appreciate the extensive help of Alexandra Papazoglou in completing the figures for this paper.

This work was supported in part by US Public Health Service grant HL-11307 and a grant of computer time from the North Carolina Supercomputing Center.

Received for publication 11 October 1991 and in final form 13 January 1992.

REFERENCES

1. Arvanitaki, A. 1942. Effects evoked in an axon by the activity of a contiguous one. *J. Neurophysiol. (Bethesda)*. 5:89–108.
2. Barr, R. C., and R. Plonsey. 1984. Propagation of excitation in idealized anisotropic two-dimensional tissue. *Biophys. J.* 45:1191–1202.
3. Beeler, G. W., and H. Reuter. 1977. Reconstruction of the action potential of ventricular myocardial fibres. *J. Physiol. (Lond.)*. 268:177–210.
4. Clark, J. W., Jr., and R. Plonsey. 1971. Fiber interaction in a nerve trunk. *Biophys. J.* 11:281–294.
5. DiFrancesco, D., and D. Noble. 1985. A model of cardiac electrical activity incorporating ionic pumps and concentration changes. *Philos. Trans. R. Soc. Lond. B Biol. Sci.* 307:353–398.
6. Drouhard, J. P., and F. A. Foberge. 1987. Revised formulation of the Hodgkin-Huxley representation of the Na^+ current in cardiac cells. *Comput. Biomed. Res.* 20:333–350.
7. Ebihara, L., and E. A. Johnson. 1981. Fast sodium current in cardiac muscle. *Biophys. J.* 32:779–790.
8. Ebihara, L. N., N. Shigeto, M. Lieberman, and E. A. Johnson. 1980. The initial inward current in spherical clusters of chick embryonic heart cells. *J. Gen. Physiol.* 75:437–456.
9. Eisenberg, R. S., V. Barcilon, and R. T. Mathias. 1979. Electrical properties of spherical syncytia. *Biophys. J.* 25:151–180.
10. Faber, D. S., and H. Korn. 1989. Electrical field effects: their relevance in central neural networks. *Physiol. Rev.* 69:821–863.
11. Geselowitz, D. B., and W. T. Miller III. 1983. A bidomain model for anisotropic cardiac muscle. *Ann. Biomed. Eng.* 11:191–206.
12. Håkanson, S. 1981. Trigeminal neuralgia treated by the injection of glycerol into the trigeminal cistern. *Neurosurgery.* 9:638–646.
13. Halter, J. A., and J. W. Clark, Jr. 1991. A distributed-parameter model of the myelinated nerve fiber. *J. Theor. Biol.* 148:345–382.
14. Henriquez, C. S., and R. Plonsey. 1990. Simulation of propagation along a cylindrical bundle of cardiac tissue. I. Mathematical formulation. *IEEE (Inst. Electr. Electron. Eng.) Trans. Biomed. Eng.* 37:850–860.
15. Henriquez, C. S., and R. Plonsey. 1990. Simulation of propagation along a cylindrical bundle of cardiac tissue. II. Results of simulation. *IEEE (Inst. Electr. Electron. Eng.) Trans. Biomed. Eng.* 37:861–875.
16. Hodgkin, A. L., and A. F. Huxley. 1952. A quantitative description of membrane current and its application to conductance and excitation in nerve. *J. Physiol. (Lond.)*. 117:500–544.
17. Joyner, R. W., B. M. Ramza, R. C. Tan, J. Matsuda, and T. T. Do. 1989. Effects of tissue geometry on initiation of a cardiac action potential. *Am. J. Physiol.* 256:H391–H403.

18. Katz, B., and O. H. Schmitt. 1940. Electric interaction between two adjacent nerve fibres. *J. Physiol. (Lond.)*. 97:471–488.

19. Kleber, A. G., and C. B. Riegger. 1987. Electrical constants of aterially perfused rabbit papillary muscle. *J. Physiol. (Lond.)*. 385:307–324.

20. Knisley, S. B., T. Maruyama, and J. W. Buchanan, Jr. 1991. Interstitial potential during propagation in bathed ventricular muscle. *Biophys. J.* 59:509–515.

21. Leon, L. J., and F. A. Roberge. 1990. A new cable model formulation based on Green's theorem. *Ann. Biomed. Eng.* 18:1–17.

22. Lewis, T., and M. A. Rothschild. 1915. The excitatory process in the dog's heart. Part I. The auricles. Part II. The ventricles. *Philos. Trans. R. Soc. Lond. B Biol. Sci.* 206:181–226.

23. Ling, G., and R. W. Gerhard. 1949. The normal membrane potentials of frog sartorius fibres. *J. Cell. Comp. Physiol.* 34:383–396.

24. Lorente de Nó, R. 1947. Analysis of the distribution of the action currents of nerves in volume conductors. Rockfeller Institute Medical Research, New York. 132:384–497.

25. Markin, V. S. 1973. Electrical interaction of parallel non-myelinated nerve fibers. III. Interaction in bundles. *Biofizika.* 18:314–321.

26. Miller, W. T., III, and D. B. Geselowitz. 1978. Simulation studies of the electrocardiogram. *Circ. Res.* 43:301–315.

27. Muler, A. L., and V. S. Markin. 1978. Electrical properties of anisotropic nerve-muscle syncytia. III. Steady form of the excitation front. *Biophysics.* 22:699–704.

28. Nelson, P. G. 1966. Interaction between spinal motoneurons of the cat. *J. Neurophysiol.* 29:275–287.

29. Plonsey, R., and R. C. Barr. 1984. Current flow patterns in two-dimensional anisotropic bisyncytia with normal and extreme conductivities. *Biophys. J.* 45:557–571.

30. Plonsey, R., and R. C. Barr. 1987. Interstitial potentials and their change with depth into cardiac tissue. *Biophys. J.* 51:547–555.

31. Plonsey, R., and R. C. Barr. 1988. Bioelectricity, A Quantitative Approach. Plenum Publishing Corp., New York.

32. Plonsey, R., C. S. Henriquez, N. Trayanova. 1988. Extracellular (volume conductor) effect on adjoining cardiac muscle electrophysiology. *Med. Biol. Eng. Comput.* 26:126–129.

33. Pollard, A. E., and R. C. Barr. 1991. Computer simulations of activation in an anatomically based model of the human ventricular conduction system. *IEEE (Inst. Electr. Electron. Eng.) Trans. Biomed. Eng.* 38:982–996.

34. Ramón, F., and J. W. Moore. 1978. Ephaptic transmission in squid giant axons. *Am. J. Physiol.* 234:C162–C169.

35. Roberge, F. A., Boucher, L., and A. Vinet. 1989. Model study of the spread of electrotonic potential in cardiac tissue. *Med. Biol. Eng. Comput.* 27:405–415.

36. Roberts, D. E., L. T. Hersh, and A. M. Scher. 1979. Influence of cardiac fiber orientation on wavefront voltage, conduction velocity, and tissue resistivity in the dog. *Circ. Res.* 44:701–712.

37. Roth, B. J. 1988. The electrical potential produced by a strand of cardiac muscle: a bidomain analysis. *Ann. Biomed. Eng.* 16:609–37.

38. Sanders, D. B. 1989. Ephaptic transmission in hemifacial spasm: a single fiber EMG study. *Muscle Nerve.* 12:690–694.

39. Schmitt, O. 1969. Biological information processing using the concept of interpenetrating domains. *In* Information Processing in the Nervous System. K. N. Leibovic, editor. Springer-Verlag, New York. 325–331.

40. Sepulveda, N. G., B. J. Roth, and J. P. Wikswo, Jr. 1989. Current injection into a two-dimensional anisotropic bidomain. *Biophys. J.* 55:987–999.

41. Spach, M. S., and R. C. Barr. 1975. Ventricular intramural and epicardial potential distributions during ventricular activation and repolarization in the intact dog. *Circ. Res.* 37:243–257.

42. Spach, M. S., W. T. Miller, III, D. B. Geselowitz, R. C. Barr, J. Kootsey, and E. A. Johnson. 1981. The discontinuous nature of propagation in normal canine cardiac muscle. *Circ. Res.* 48:39–54.

43. Suenson, M. 1984. Ephaptic impulse transmission between ventricular myocardial cells in vitro. *Acta Physiol. Scand.* 120:445–455.

44. Taccardi, B., L. S. Green, P. R. Ershler, and R. L. Lux. 1989. Epicardial potential mapping: effects of conducting media. *Circulation.* 80:II-134.

45. Tan, R. C., and R. W. Joyner. 1990. Electrotonic influences on action potentials from isolated ventricular cells. *Circ. Res.* 67:1071–1081.

46. Tuang, L. 1978. A bi-domain model for describing ischemic myocardial d-c potentials. Ph.D. dissertation. Massachusetts Institute of Technology, Cambridge, MA.

47. Vander Ark, C. R., and E. W. Reynolds, Jr. 1970. An experimental study of propagated electrical activity in the canine heart. *Circ. Res.* 26:451–460.

48. Wikswo, J. P., Jr., T. A. Wisialowski, W. A. Altemeier, J. R. Balser, H. A. Kopelman, and D. M. Roden. 1991. Virtual cathode effects during stimulation of cardiac muscle. Two-dimensional in vivo experiments. *Circ. Res.* 68:513–30.